Prediction of turbulent fluid flow and heat transfer in a rotating periodical two-pass square duct

Received March 1997
Revised October 1997
Accepted January 1998

J.J. Hwang, T.Y. Lia and S.H. Chen
Department of Mechanical Engineering, Chung-Hua University, Hsinchu, Taiwan, Republic of China

Nomenclature

c_p = Specific heat at constant pressure
De = Channel hydraulic diameter or channel height
Gr = Rotational Grashof number, $(\Omega^2 De)\ \beta q_w De^4/(k_f \upsilon^2)$
h = Local heat transfer coefficient, $q_w/(T_w - T_b)$
k = Turbulent kinetic energy
k_f = Air thermal conductivity
L_x = Module length (in X direction), i.e. $20De$
L_y = Module height (in Y direction), i.e. De
L_z = Module width (in Z direction), i.e. $3De$
$\dot{m}$ = Mass flow rate through the duct
Nu = Local Nusselt number, hDe/k_f
Nu_x = Local (single) wall-averaged Nusselt number
$\overline{Nu}_x$ = Local peripherally averaged Nusselt number
$\overline{Nu}_s$ = Fully developed Nusselt number for stationary-straight-pipe flow, i.e. $0.023\ Re^{0.8}\mathrm{Pr}^{0.4}$
p = Pressure
Pe = Peclet number
Pr, Pr_t = Laminar and turbulent Prandtl number respectively
Q = Total heat input into a module
q_w = Wall heat transfer
Re = Reynolds number, $\bar{u}De/v$
Re_Ω = Rotational Reynolds number, $\Omega De^2/v$
Ro = Rotation number, $Re_\Omega/Re = \Omega De/\bar{u}$
T = Temperature of air
T_b = Local bulk mean temperature of air
T_r = Reference temperature
T_w = Local wall temperature
u, v, w = Local mean-velocity components in x, y, and z directions respectively
$\bar{u}$ = Average mean velocity in the duct
X, Y, Z = Dimensionless rectangular coordinate, x/De, y/De, and z/De
x, y, z = Rectangular coordinate, see Figure 2
x_o = Radial distance from rotating axis to the two-pass channel, $49De$, see Figure 2
y^+ = Dimensionless distance, $\delta\sqrt{\tau_w/\rho/v}$

Greek symbols

Ω = Angular velocity of rotation
β = Coefficient of thermal expansion
δ = Distance between the wall and the nearest-wall node
σ_k, σ_e = Prandtl numbers for k and ε equations
ε = Rate of dissipation of turbulent kinetic energy
γ = Air enthalpy rise parameter, $Q/(\dot{m}c_p L_z)$
η = Pressure drop parameter
ϑ = Dimensionless temperature, $(T - T_r)/(q_w De/k_f)$
τ_w = Wall shear stress
μ, μ_t = Laminar and turbulent viscosity respectively
υ, v_t = Laminar and turbulent kinematic viscosity respectively
ρ = Air density

Subscripts

b = Bulk mean
s = Smooth or stationary
w = Wall
x = x-dependence

Superscripts

$\hat{}$ = Periodicity
$-$ = Average

Support for this work was provided by the National Science Council of the Republic of China under contract No. NSC 85-2212-E-216-003.

International Journal of Numerical Methods for Heat & Fluid Flow
Vol. 8 No. 5, 1998, pp. 519–538.

Introduction

The increase in the turbine inlet temperature of the gas turbine engines is an urgent need today to obtain a higher efficiency in the aircraft engines. Parallel with the development of blade materials working in high temperature, several ways of cooling blades are widely used in the modern engines. In general, film cooling is imposed on the external surfaces of the blades while forced-convection cooling is employed inside the blades by means of cooling passages. The present study pertains to the latter, i.e. flow and heat transfer in the internal cooling passages. As shown in Figure 1, the flow passages in an actual blade of a typical turbine engine is idealized as a multiple-pass serpentine-type channel. The thermal behavior within such passages is influenced by several factors, such as the presence of sharp 180° bends and the rotational induced Coriolis force. In addition, a strong temperature gradient, if present, creates a centrifugal buoyancy effect that causes complex secondary flow patterns, and consequently modifies heat transfer coefficient. The ability to predict how wall heat transfer coefficients are affected by rotation in serpentine ducts is thus of considerable value to engine designers.

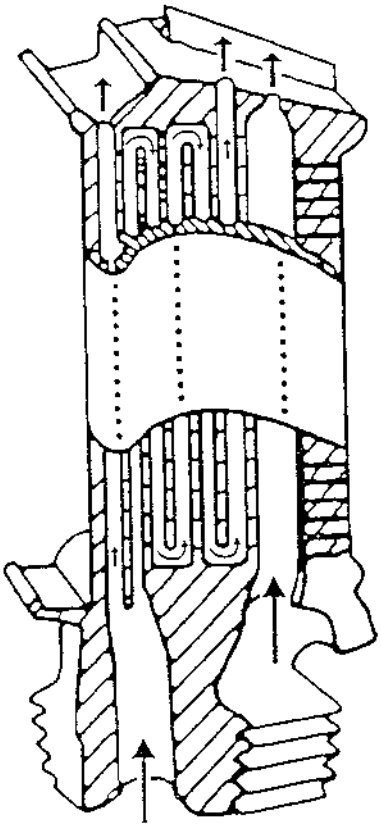

Figure 1.
Cooling concepts of the modern turbine blade with serpentine cooling passages

Majumdar *et al.*[1] used the standard *k-e* model to resolve the parabolic turbulent fluid flow in a rotating duct, but unsatisfactory results were obtained for moderate to high rotation number. It was therefore suggesting the need for modifications to account for the rotational effects. Later, by using Coriolis modified turbulence models, Howard *et al.*[2] got better predictions of fully developed rotating mean flow and turbulent viscosity. Launder *et al.*[3] developed a second-moment closure turbulence model and satisfactorily predicted rotating fully developed flow without heat transfer. In respect of heated channels, Iacovides and Launder[4] further predicted fully developed turbulent flow and heat transfer in rotating rectangular channels. Except in the immediate vicinity of the wall, the standard *k-e* turbulence model was employed; across the near-wall sublayer, the damping of turbulence was modeled by means of a low-*Re*, one-equation model. However, due to the presence of entrance and centrifugal-buoyancy effects in the available experimental data, a theory-data match was difficult. Recently, Prakash and Zerkle[5], and Tekriwal[6] predicted heat transfer results with a high Reynolds number *k-e* model including thermal buoyancy effects in the momentum equations. A reasonably qualitative agreement with experimental profiles of local Nusselt number was obtained, but the trailing side Nusselt number was still significantly underestimated. More recent, detailed comparisons were made by Bo *et al.*[7] among the three turbulence models, namely *k-e*/one equation EVM (eddy viscosity model), low-*Re k-e* EVM, and low-*Re* ASM (algebraic Reynolds stress model) in predicting turbulent fluid flow and heat transfer in a rotating duct by taking buoyancy effects into account. It was found that the low-*Re* ASM model predictions were in encouragingly close agreement with the experiments of Wagner *et al.*[8], whereas the low-*Re k-e* EVM provided spectacularly unrealistic flow behavior near the suction side wall. Dutta *et al.*[9] used the *k-e*/two-equation turbulence model to predict heat transfer from the leading and trailing sides of a rotating square channel with radially outward flow. Satisfactory results compared with the previous experiments[8,10] were achieved by inclusion of the modified rotational turbulence generation terms in the momentum and *k-e* transport equations.

From the above discussion of literature review, it indicates that the most numerical investigations, indeed, only deal with developing or fully developed flows in a single straight channel with radially outward flow. In addition, the local heat transfer characteristics are largely dependent on the flow direction in radially rotating serpentine channels[11]. However, the numerical efforts containing information about the heat transfer as well as the fluid flow in a rotating multiple-pass channel are rather sparse. This motivates the present study which is to direct our goal to predict turbulent flow and heat transfer in a multiple-pass square channel with orthogonal rotating conditions. The local heat transfer characteristics along a rotating serpentine flow passage is nearly periodic after the first turn of a multiple-pass channel[12]. Here, we focus our attention on a periodically fully developed situation, which assumes that the flow and heat transfer characteristics repeat themselves cyclically from the

entrance of the channel to the next. This assumption allows the calculation domain to be limited to the region across a two-pass (radial-inward and radial-outward) channel, as shown in Figure 2. It is believed that a substantial body of numerical data, as done by the present work, is highly required to accurately predict the heat transfer coefficient, flow field, and flow regime in this important area of gas turbine blade internal cooling problems.

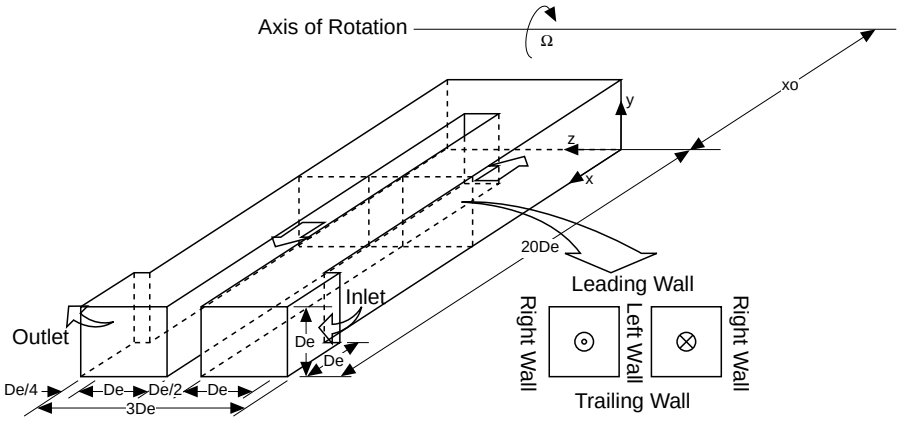

Figure 2.
Sketch of coordinate system, and dimensions of the periodic two-pass module

Numerical and turbulence models

Governing equations

Figure 2 shows the physical configuration of the test module of the periodic two-pass square channel. The test module has 20 channel hydraulic diameters in length, three in width, and one in height, and rotates at a constant angular speed Ω about the axis normal to the main flow direction. The distance from the rotation axis to the module is 49 De (x_0). This module consists of two 90° miter junctions at the module inlet and outlet, a radial-inward straight channel, a radial-outward straight channel, and a 180° sharp bend, which is to simulate the periodical region of a typical serpentine multiple-pass cooling passage of the turbine blade. The main stream enters the channel from an entrance with a 90° miter, flows through the radial-inward-flow channel, then turns sharply with a 180° bend to the radial-outward-flow channel, and finally exits this channel from another 90° miter. The u, v, and w are the velocity components of the x, y, and z directions. The labeling order of each wall of this two pass channel is also given in Figure 2. The orientation of "left", and "right" is chosen as one follows the mainstream direction passing through the entire passage. To facilitate the analysis, the flow is assumed to be steady, and of constant properties, and viscous dissipation and compression works are ignored. Gravitational force is neglected for its small magnitude compared to the rotation-induced centrifugal force. The Boussinesq approximation of a linear density-temperature relation, $\Delta\rho/\rho = \beta(\Delta T)$ is invoked for the consideration of centrifugal-buoyancy.

Basically, all flow variables that repeat cyclically over the length of computational module can be represent as follows[13].

$$\varphi(x, y, z) = \varphi(x, y, z + L_z) \tag{1}$$

where φ could be any velocity component (u, v, w), the turbulent kinetic energy (k), or the turbulent dissipation rate (ε). As for the pressure, it can be decomposed as

$$p = -\eta z + \hat{p} \tag{2}$$

where $\hat{p}$ is cyclic (i.e. abides by above equation) while the term ηz is related to the net pressure loss over the computation module. Practically, in a periodic analysis, the flow rate (or Reynolds number) is not known in prior. Solution for a given flow rate is achieved by iteratively updating the value of the global pressure gradient parameter, η, until convergence is reached. That is for a given value of η, there will be a corresponding value of the flow rate in the channel. Patankar *et al.*[13] also discussed the formulation of the thermal problem in a periodic framework. The temperature for field under the uniform-heat-flux conditions can be expressed as

$$T = \gamma z + \hat{T} \tag{3}$$

where $\hat{T}$ is cyclic while the first term on the right-hand side is related to the net heat gain and can be obtained from an overall heat balance, i.e.

$$\gamma = Q / (L_z \bullet \dot{m} \bullet c_p) \tag{4}$$

where Q is the total heat input over the module, $\dot{m}$ the mass flow rate, and c_p the specific heat. The corresponding governing equations of mass, momentum and energy are:

$$\text{div}(\boldsymbol{u}) = 0 \tag{5}$$

$$\rho\,\text{div}(\boldsymbol{u}\,u) = -\frac{\partial \hat{p}}{\partial x} + 2\rho\Omega v - \rho\Omega^2(x+x_o)\beta\hat{T} + \text{div}[(\mu+\mu_t)\text{grad}(u)] \tag{6}$$

$$\rho\,\text{div}(\boldsymbol{u}\,v) = -\frac{\partial \hat{p}}{\partial y} - 2\rho\Omega u - \rho\Omega^2 y\beta\hat{T} + \text{div}[(\mu+\mu_t)\text{grad}(v)] \tag{7}$$

$$\rho\,\text{div}(\boldsymbol{u}\,w) = -\frac{\partial \hat{p}}{\partial z} + \eta + \text{div}[(\mu+\mu_t)\,\text{grad}(w)] \tag{8}$$

$$\rho \, \mathrm{div}\,(\boldsymbol{u}\,\hat{T}) = -\rho\, u\, \gamma + \mathrm{div}\,[(\frac{\mu}{Pr} + \frac{\mu_t}{Pr_t})\,\mathrm{grad}(\hat{T})] \tag{9}$$

In equations (5)-(9), the symbols (div) and (grad) designate the divergence and the gradient operators. The second and third terms on the right hand side of equations (6) and (7) represent the rotational induced Coriolis forces and buoyancy forces respectively. The variable symbol μ_t represents the turbulent viscosity, and Pr_t designates the turbulent Prandtl number. The turbulent Prandtl number is usually constant and is taken $Pr_t = 0.86$ here.

Turbulence model

The turbulent viscosity is varied throughout the flow field and obtained from the turbulent kinetic energy (k) and the rate of the dissipation of turbulent energy (ε)[14]. Specifically,

$$\mu_t = \rho\, C_\mu\, k^2 / \varepsilon \tag{10}$$

The k and ε are obtained from the following transport equations:

$$\rho \, \mathrm{div}\,(\boldsymbol{u}\, k) = \mathrm{div}\,[(\mu_t/\sigma_k)\,\mathrm{grad}\,(k)] + G - \rho\varepsilon + G_c + G_b \tag{11}$$

$$\rho \, \mathrm{div}\,(\boldsymbol{u}\, \varepsilon) = \mathrm{div}[(\mu_t/\sigma_\varepsilon)\mathrm{grad}(\varepsilon\, k)] + (C_1 G + G_c + C_3\, G_b)(\varepsilon / k) - C_2 \rho\, \varepsilon^2/k \tag{12}$$

where G is the usual Reynolds stress turbulence production term [8,14]. The buoyancy and Coriolis generated turbulence production terms are taken as

$$G_b = (\mu_t / \mathrm{Pr_t})\, \Omega^2\, (x + x_o)\, \beta\, (\partial \hat{T} / \partial x) \tag{13}$$

$$G_c = 9 \mu_t\, \Omega (\partial u / \partial y) \tag{14}$$

The buoyancy generation term, G_b, is due to Dutta *et al.*[9] and the related constant C_3 is taken as 0.9, which arises from the Boussinesq approximation of the velocity-temperature cross-correlation[15]. The Coriolis modified term, G_c, is included from Howard *et al.*[2]. In general, G_c is positive near the trailing wall and negative near the leading wall in the radial-outward-flow channel, while the reverse is true in the radial-inward-flow channel. A positive G_c enhances turbulence and a negative G_c suppresses turbulence. The boundary layer velocity profile near the wall means that G_c has a stronger influence at near wall region than G_b for flow and heat transfer situations to be considered. It is found that G_b has an influence up to 9.0 percent on heat transfer for the radial outward flow, but less than a 6.0 percent influence for the radial-inward flow. The other constants above have the following values : $\sigma_k = 1.0$, $\sigma_\varepsilon = 1.31$, $C_1 = 1.44$, $C_2 = 1.92$, $C_\mu = 0.09$.

The k-ε equations provided above apply in the fully turbulent regions away from the walls where laminar effects can be neglected. To bridge this outer solution to the wall, the relevant equations have to be integrated across the viscous sublayer. The wall functions, i.e. the log-law of the wall, are the outcome

of such semi-empirical integrations. The purpose of these functions is to relate the wall shear and heat flux to the velocity and the temperature difference between the wall and the near-wall node[14].

Boundary conditions and investigated parameters

No inlet and outlet conditions are required for a periodical analysis. At the walls, no-slip condition is used in conjunction with the wall functions. For temperature equation, since the heat flux is prescribed at the wall, the wall functions are used to determine the wall temperature from the computed near-wall temperature. The difference between the wall temperature and the local bulk temperature is then used to calculate the local heat transfer coefficient.

Since the rotational buoyancy effect caused by the density variation is interesting in the present work, a dimensionless buoyancy parameter is therefore developed to simplify this problem. By using scale analysis, the dimensionless buoyancy parameter can be deduced by taking the ratio of the third term on the right-had side of equation (6) and the convection term of the equation (6):

$$\Omega^2 (x + x_o)\, \beta\, \hat{T} / (\bar{u}^2 / De) = [(\Omega^2 De)\, \beta\, \Delta T\, De^3 / \nu^2][(x + x_o) / De][(\hat{T} / \Delta T)] / Re^2 = Gr / Re^2 (X + X_o)\, \hat{\vartheta} \quad (15)$$

From the above reduction, the buoyancy parameter is therefore expressed as $Gr/Re^2\ (X + X_0)$, which is, indeed, equivalent to the parameter of $(\Delta\rho/\rho)[(x + x_0)/De](\Omega De/\bar{u})^2$ given by Wagner *et al.*[15]. In the present computation, the buoyancy parameter Gr/Re^2 is varied from 2.4×10^{-3} to 1.12×10^{-2} depending on the quantity of heat input to the channel. The buoyancy-free case (i.e. $Gr/Re^2 = 0$) is also conducted for comparison. The radial distance from the rotational axis to the channel is $x_0 = 49\ De$. The Reynolds number and rotational number are kept at values of 25,000, and 0.12 respectively.

Computational details

The control-volume-based finite difference method described by Patankar[16] is employed to solve the governing equations described above. It uses the primitive variables as unknowns, a staggered grid, and SIMPLER pressure correction algorithm are employed. In addition, to reduce numerical oscillation during iteration for $|\mathrm{Pe}| \fallingdotseq 2$, the finite difference scheme of smooth hybrid central/skew upstream difference scheme (SCSUDS) is employed in this work, the details of which can be found in Liou *et al.*[17]. The set of the differential equations over the entire region of interest is solved by obtaining new values for any desired variables, taking into account the latest known estimated values of the variable from the neighboring nodes. One iteration process is complete when, in line-by-line technique, all lines in a direction have been accounted for. Solutions are considered to be converged at each test condition after the ratio of

residual source (including mass, momentum, and thermal and turbulent kinetic energy) to the maximum flux across a control surface is below 10^{-3}.

In this problem, most of the real action is found around the 180° turns and near all solid surfaces and, therefore, nodes are clustered in these regions in order to resolve the strong gradients present there. However, owing to the conflicting requirement of keeping near-wall y^+ reasonably large, the grid could not be refined excessively around the sharp turns. To keep this issue, the range of the y^+ encountered on different surfaces is checked and listed in Table I. It is expected that, as the velocities are quite small near the corners of the sharp turns, the y^+ values become quite small around these regions. Also, on the right (or left) wall adjacent to the sharp turn, the y^+ values are small because of the flow recirculation. Although the general laminar limits imposed on the wall-function expression is $y^+ > 30$, the use of the wall-functions is not harmful as long as the locations of low y^+ are not too many. All computations are performed on $144 \times 96 \times 37$ straight-line grids in the present work. Additional runs for the coarser meshes, $96 \times 60 \times 24$, and the finer meshes, $186 \times 132 \times 60$, are taken for a check of grid independence. The parameters used to check the grid independence are axial velocity profiles, temperature profiles, and the local Nusselt number distributions. A comparison of the results of the two grid sizes, $144 \times 96 \times 37$, and $186 \times 132 \times 60$, shows that the maximum discrepancies in the axial velocity and temperature profiles are 1.2 and 1.6 percent respectively, for the stationary condition ($Ro = 0$). Computations for $Ro = 0.12$ are also conducted and the results indicate a maximum change of 1.9 percent in Nusselt number distribution between the solutions of $144 \times 96 \times 37$, and $186 \times 132 \times 60$ grids. These changes are so small that the accuracy of the solutions on a $144 \times 96 \times 37$ grid is deemed satisfactory. Numerical computation of the periodically fully developed flow is rendered difficult by the fact that no boundary information is available. Partly due to this reason, the code takes about 8,000-12,000 iterations for convergence. On Convex-C3840, this translated to about 10 hours of CPU time.

Variation of y^+, Re = 25,000, Ro = 0.12, Gr = 0

Pressure side	30-110
Suction side	24-62
Right (or left) straight wall	18-100
Turn region	14-60

Table I.
The range of y^+ on the difference surfaces of the two-pass channel

Results and discussion

Development of axial mean velocity and turbulent intensity

Figures 3 (a)-(c) depict the axial development of the mean velocity in the rotating two-pass square channel with three different rotational buoyancy parameters, i.e. $Gr/Re^2 = 0$, 0.0024, and 0.0112. The Reynolds number and the

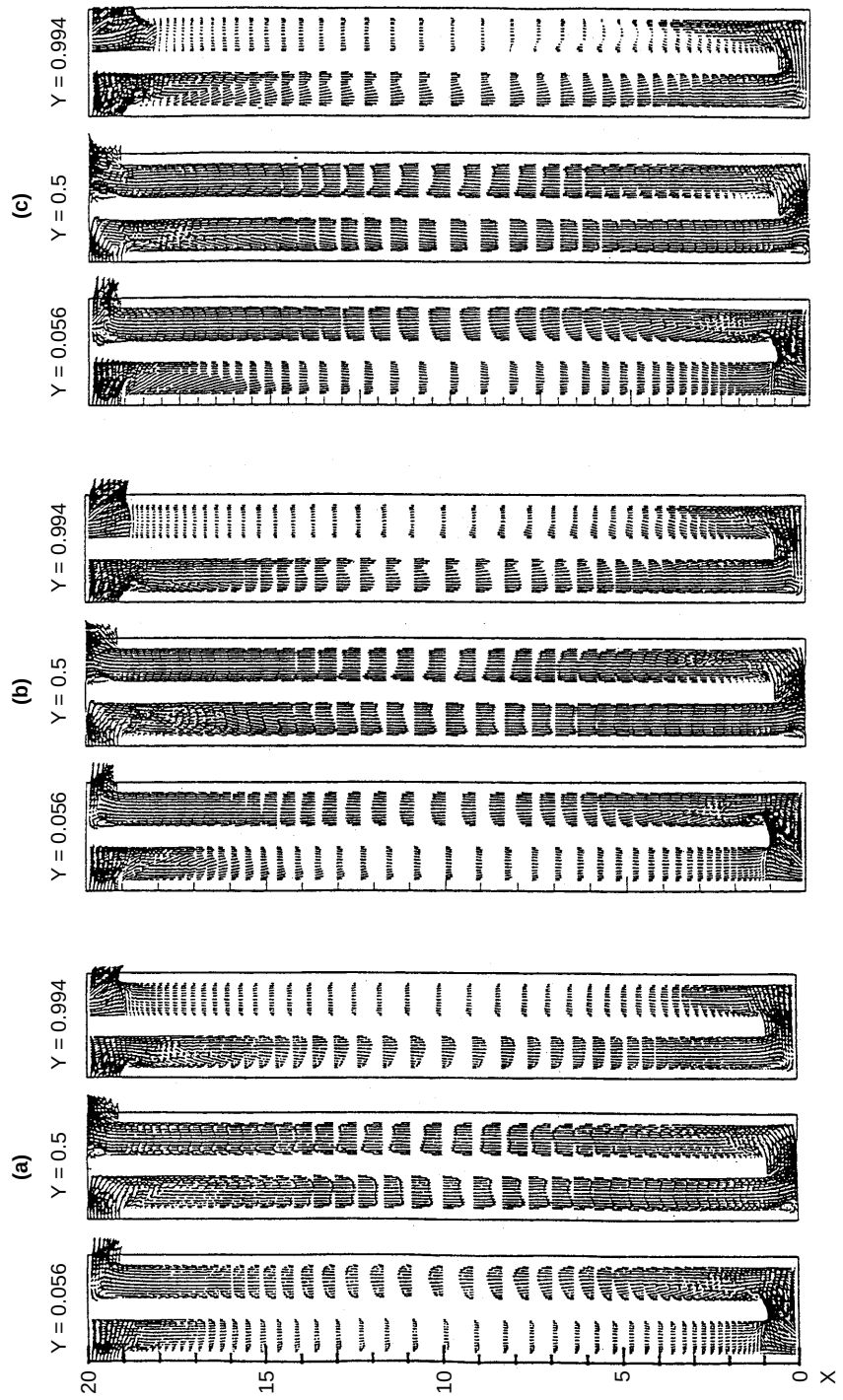

Figure 3.
Development of mean-velocity vectors (u, w) along the two-pass duct, (a) $Gr/Re^2 = 0$, (b) $Gr/Re^2 = 0.0024$, (c) $Gr/Re^2 = 0.0112$

rotation number are fixed at Re = 25,000, and Ro = 0.12 respectively. Three sectional views shown in each plot are respectively cutting across the planes near leading side (Y = 0.944), near trailing side (Y = 0.056) and of channel center (Y = 0.5). The vectors are composed of the mean-velocity components in the x- and z- directions. It is observed from these graphs that, in the radial-inward-flow channel, the magnitude of streamwise velocity near the leading wall (Y = 0.944) is significantly higher than that near the trailing wall (Y = 0.056) due to the rotational induced Coriolis force. An opposed trend is found in the radial-outward-flow channel. In the buoyancy-free case (i.e., Gr/Re^2 = 0, Figure 3(a), regardless of the flow direction, the flow patterns near the leading wall of the radial-inward-flow channel are largely identical to those near the trailing wall of the radial-outward channel, if the streamwise distance relative the upstream sharp turn is the same, and vice versa. This is very reasonable because the rotational induced buoyancy is neglected and, therefore, only the opposite direction of the Coriolis force acting on these two channels, which is directed at the trailing wall and leading wall for the radial-outward-flow and radial-outward-flow channels respectively. When the buoyancy force of Gr/Re^2 = 0.0024 is acting on the fluid, the magnitude of streamwise velocity near the trailing wall for both the radial-inward-flow and radial-outward-flow channels becomes larger than that of the buoyancy-free channels. The former is because, in the radial-inward-flow channel, the centrifugal buoyancy parallels to the main-flow direction, which favors the relatively hot fluid near the trailing face (will be shown later) and, in turn, accelerates the fluid near the trailing wall. In the radial-outward-flow channel, the centrifugal buoyancy directs against the main flow direction, which is greater on the fluid near the leading face (hot fluid) and smaller on the fluid near the trailing face; consequently, due to the imbalance of the force, the radial velocity of the fluid decreases near the leading face and increases near the trailing wall., The above phenomena become more significant as the rotating buoyancy inertia is further increased. It is highly noted in Figure 3(c) that for Gr/Re^2 = 0.0112, the flow reversal is observed after about X = 4.5 near the leading wall in the radial-outward-flow channel. Similar phenomenon was observed by Prakash and Zerkle[5] for a single-pass radially outward channel with fully developed inlet conditions at high rotating speeds and/or density ratios.

For simplicity, the axial mean-velocity profiles along the radial-inward-flow and radial-outward-flow channel centerlines (Z = 0.5, and 1.75) at some selected axial stations are depicted in Figure 4. The profiles of turbulent kinetic energy are also shown in this figure. It is seen from this figure that the centrifugal-buoyancy effect tends to sharpen the mean-velocity curves of the radial-outward flow, but flatten those of the radial-inward flow. As for the turbulent kinetic energy, the distributions are rather uniform in core flow region for the buoyancy-free case both in radial-inward and -outward-flow channels. At the axial station of X = 10, and 18 in the radial-outward-flow channel, the turbulent kinetic energy near the leading side is greatly enhanced by the buoyancy parameter. This is because relatively hot fluid near the leading wall flows

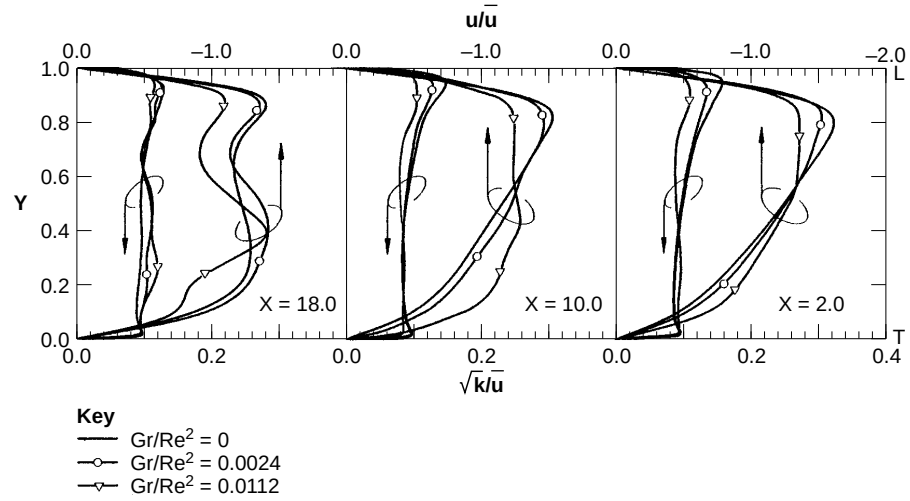

Figure 4(a). Effect of centrifugal buoyancy on the streamwise mean-velocity and turbulent kinetic energy distributions at several axial stations for radial-inward flow

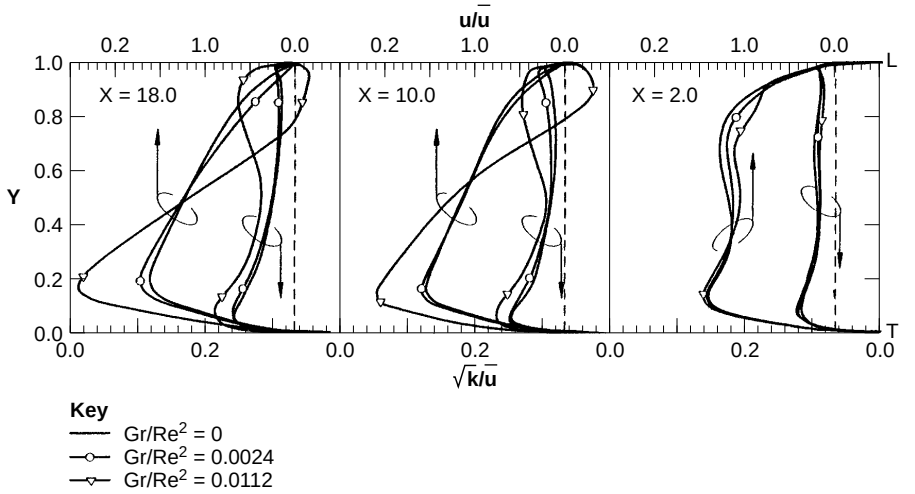

Figure 4(b). Effect of centrifugal buoyancy on the streamwise mean-velocity and turbulent kinetic energy distributions at several axial stations for radial-outward flow

inward toward the axis of rotation, and the coolant flow is outward; therefore, the strong shear gradient near the leading wall caused by this counter-flow situation generates a higher near-wall turbulence kinetic energy. In contrast, in the radial-inward-flow channel, the turbulent kinetic energy is slightly decreased with rotational buoyancy because of the less shear gradient.

Cross-flow vectors and iso-speed contours

Figures 5 and 6 respectively display the projection of the cross-flow velocity vectors and the iso-speed contours of the streamwise mean velocity at the channel cross-stream planes of $X = 10$ for three different buoyancy parameters. All plots are viewed in the negative X (radial-inward) direction. The solid curves

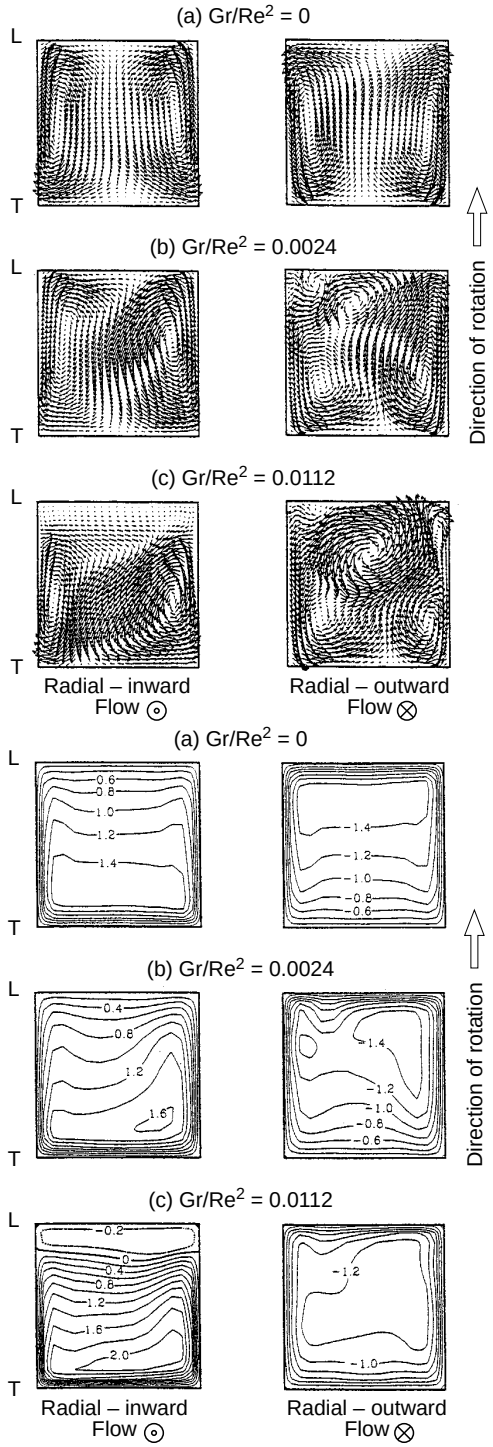

Figure 5.
Effect of centrifugal buoyancy on the secondary-flow vectors at several axial stations for the radial-inward and -outward-flow channels, (a) $Gr/Re^2 = 0$, (b) $Gr/Re^2 = 0.0024$, (c) $Gr/Re^2 = 0.0112$

Figure 6.
Effect of centrifugal buoyancy on the streamwise iso-speed contours at several axial stations for the radial-inward and -outward-flow channels, (a) $Gr/Re^2 = 0$, (b) $Gr/Re^2 = 0.0024$, (c) $Gr/Re^2 = 0.0112$ (the scales on the iso-speed contour means the magnitude of the ratio of $u/\overline{u}$)

of the iso-speed counters correspond to the forward flow while the dotted curves correspond to the reversed flow. In the radial-inward-flow channel, the buoyancy-free flow ($Gr/Re^2 = 0$) has a pair of vortices induced by the Coriolis force, which circulates from the trailing wall to the leading wall through the center of the duct and then returns back along the side walls. This vortex-pair is slightly deflected to the left wall due to the centrifugal-inertia effect of flow turning around the upstream 180° sharp turn. This phenomenon is also found in the iso-speed mainstream contours which show that the largest velocity core is slightly placed to the corner formed by the leading and left walls. When a lower buoyancy of $Gr/Re^2 = 0.0024$ acts on the radial-inward flow, the vortex-pair is evidently distorted. An additional vortex-pair is bifurcated near the corner formed by the leading and left walls. As the rotational buoyancy is further increased, $Gr/Re^2 = 0.0112$, the cross-flow structure seems to be more complex, and the departure of the magnitude of mainstream velocity becomes less between the flow near the leading and trailing walls. In the radial-outward flow, the mainstream contours and the cross-flow vectors are largely identical to those in the radial-inward flows regardless the flow direction. This circumstance, however, does not keep true when the centrifugal buoyancy arises in the heated duct. At a higher buoyancy force, $Gr/Re^2 = 0.0112$, the Coriolis-induced vortex-pair is significantly placed to the trailing wall (Figure 6 (c)) and the fluid near the leading wall flows upstream (Figure 5 (c)) with very small cross-flow intensity (Figure 6 (c)).

Isotherms and local heat transfer coefficients

Figure 7 shows a comparison of the isotherms and the distributions of the local Nusselt number ratio between buoyancy-free and buoyancy-driven flows at the axial station of $X = 10$. The local Nusselt number is normalized by the well-known Dittus-Bolter correlation for fully developed pipe flow in stationary conditions. In general, the strength of the thermal-field distribution is in contrast to that of the fluid. The region of high mean-velocity, where most heat is removed convectively away by the fluid, is the region of lower temperature. In all plots, the local heat transfer coefficients diminish at all four corners of the square flow cross section due to the flow velocity diminishing in both the main and cross flow directions. At $Gr/Re^2 = 0$, the cold fluid core is forced to the leading wall in the radial-inward-flow duct; while an opposed trend is observed for the radial-outward-flow duct. In comparison of the buoyancy-free results, the fluid temperature distribution for $Gr/Re^2 = 0.0112$ in the core-region of the radial-inward flow is more uniform, which results in less departure of the magnitude in the local Nusselt number ratio between the leading and trailing walls. Conversely, in the radial-outward-flow duct, a significant temperature rise of the fluid near the leading wall is caused by slower reversed fluid movement due to the strong against buoyancy, which largely deteriorates the heat transfer on the leading wall. However, this deterioration in heat transfer is somewhat compensated by the enhancement in near-wall turbulence kinetic energy (Figure 4). Therefore, at this station, the local Nusselt number only

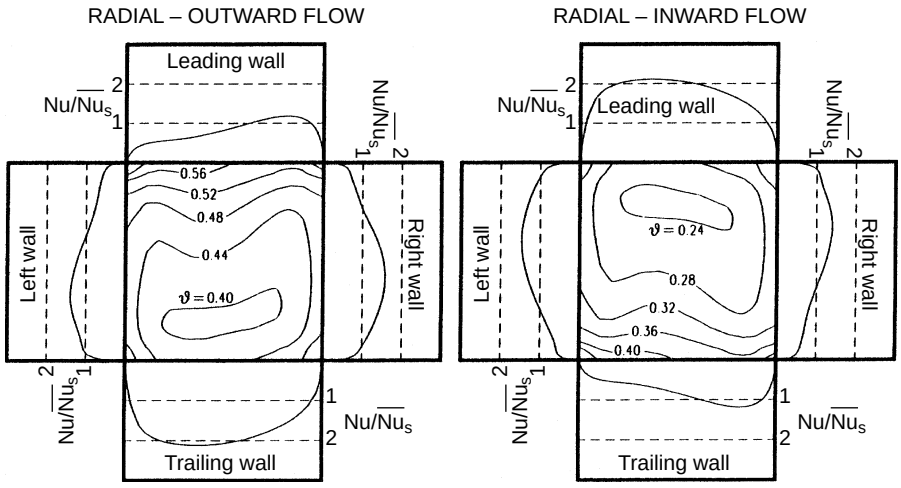

Figure 7(a).
Fluid isothermal contours and local Nusselt number distributions along the duct circumference for $Gr/Re^2 = 0$

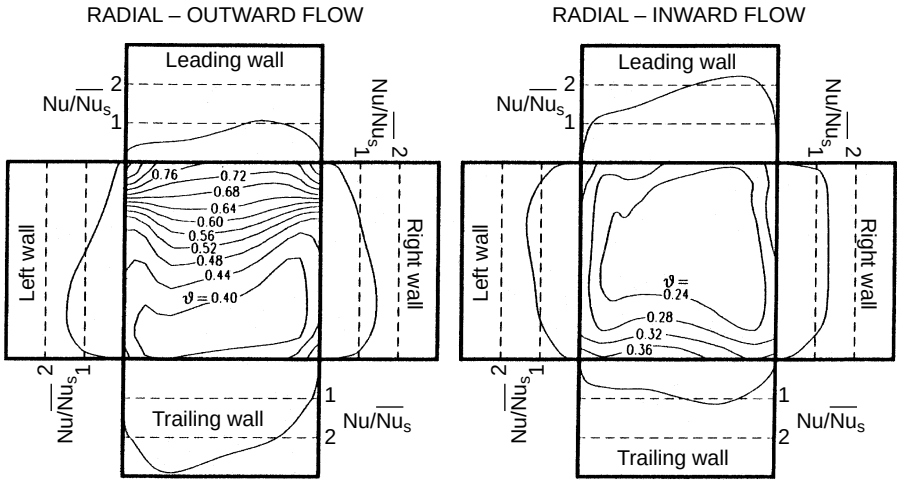

Figure 7(b).
Fluid isothermal contours and local Nusselt number distributions along the duct circumference for $Gr/Re^2 = 0.0112$

slightly decreases on the leading wall as the buoyancy parameter Gr/Re^2 increases from 0 to 0.0112. In contrast, both the mean- and fluctuating-transportation effects mentioned above benefit the heat transfer augmentation near the trailing surface of the radially outward flow (Figures 4 and 5).

Distributions of wall averaged Nusselt number

The axial variation of the Nusselt number ratio along the four duct walls for different buoyancy parameters is shown in Figure 8. The Reynolds number and the rotation number are fixed at Re = 25,000, and Ro = 0.12 respectively. Adjacent the 180° turn, regardless of the flow direction, the heat transfer ratio distributions along the four duct walls are nearly independent of the buoyancy

parameters investigated due to the rather strong entrance effect relative to the buoyancy effect. As flow turns around the 180° bend, a strong cross-flow intensity as well as turbulence intensity could be introduced due to centrifugal inertia originated by flow curvature, flow separation, flow impingement, and their interaction[18,19], which will largely enhance the heat transfer in the entrance region. Therefore, the buoyancy effect becomes significant only when the entrance effect is gradually diminished downstream. In the buoyancy-free channel, the heat transfer distributions along the pressure side and the suction side are totally identical between the radial-inward and -outward-flow ducts. In addition, the local Nusselt number ratio distribution between the right and left duct walls is significantly different, which is attributed to the aforementioned flow behavior of turning around the 180° sharp bend. These two distributions,

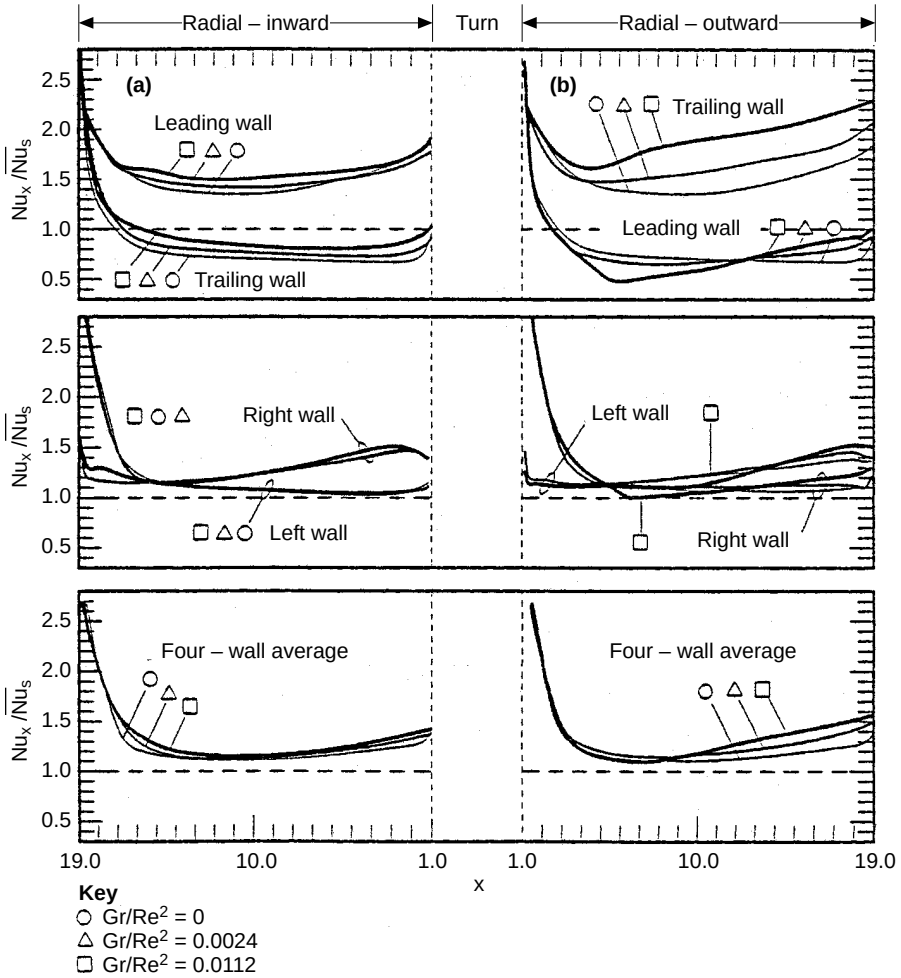

Figure 8.
Effect of rotational buoyancy on the local wall-averaged Nusselt number distributions along the radial-inward and radial-outward-flow channels

however, could be interchanged with each other between the radial-inward-flow channel and the radial-outward-flow channel. Both these two facts imply that the heat transfer characteristic is dominant by the effects of the behavior of flow turning around the 180° bend and the rotational Coriolis force. They generate largely identical mean-flow (including main and secondary flows, Figures 3, 5 and 6), turbulent-flow (Figure 4), and thermal fields (Figure 7) for the radial-inward and radial-outward-flow channels.

As for the buoyancy-driven flow, owing to the different effects of the rotational buoyancy in the co-flowing radial-inward-flow duct and in the counter-flowing radial-outward-flow duct, the discrepancy in heat transfer between the outward and inward flowing channels is anticipated. In the radial-inward-flow channel, the local Nusselt number ratios along both the trailing and leading sides increase slightly by increasing the buoyancy parameter. This buoyancy-affected thermal behavior can be grouped into several factors. First, rotating buoyancy augments the cross-flow intensity and, in turn, enhances heat transfer. As given in Figure 6, the cross-flow structure for the buoyancy-assisted flow is more complex than that for the buoyancy-free flow. Second, the buoyancy alternates the convective ability through changing the magnitude of the near-wall mean-velocity. The assisted buoyancy increases the streamwise mean-velocity near the trailing side but retards it near the leading side (Figure 4, X = 10, and 18); consequently, it augments the trailing-wall heat transfer and deteriorates the leading-wall heat transfer. Third, relatively weaker shear layer caused by the coincident direction of the main and buoyancy-assisted flows reduces the generation of near-wall turbulence kinetic energy (Figure 4); hence a reduction in heat transfer. Among these three factors, the first is in favor of the enhancement of heat transfer on the both trailing and leading walls, whereas the last one decreases both. As for the second factor, it could reduce the discrepancy in heat transfer between the leading and trailing walls. Obviously, the combination of these three effects results in a slight enhancement in heat transfer due to rotating buoyancy.

In the radial-outward-flow channel, the changes of local Nusselt number distribution due to rotating buoyancy are more significant than those in the radial-inward flow channel, especially for Gr/Re^2 = 0.0112. In the case of Gr/Re^2 = 0.0112, apparent bumpers for the distributions of local Nusselt number ratio are observed for the four duct walls due to the initiation of the flow reversal near the leading wall (Figure 3). The steep increase in Nusselt number ratio along the trailing wall after about X = 4.0 is mainly due to a sharp increase of the mean-flow velocity (Figure 3). Along the leading wall, the distribution of the Nusselt number ratio falls to a local minimum with about 50 percent of the stationary-fully-developed-flow value due to the relatively stagnant fluid near the leading wall. It then increases downstream because of the enhancement of turbulence transports caused by the strong shear gradient (Figure 4).

Attention is now turning to the channel averaged results. Comparing with buoyancy-free channel results, the channel with a finite straight length of 18 De in the highest rotational buoyancy investigated, say Gr/Re^2 = 0.0112, enhances

about 5 percent and 13 percent in channel-averaged heat transfer for the radial-inward and radial-outward-flow channels respectively. This little effect of rotational buoyancy is because the thermal conditions have been fully developed by the complex secondary (mean) and turbulent flows caused by the Coriolis, the mechanisms of flow turning around the 180° bend, and their interaction. Therefore, an additional disturbance caused by rotational buoyancy could only redistribute the local heat transfer through alternating the mean and turbulent transportation, but no longer augments significantly the overall performance.

As mentioned above, the reversed-flow phenomenon in the internal cooling passages will adversely affect the heat transfer performance of the cooling channels; therefore, it is very important to know the radial location from which the flow separates, which can provide useful information about the thermal-control design of the cooling channels. Figure 9 shows the relationship between the buoyancy parameter and the radial distance (X) for initiation of flow separation in the radial-outward-flow channel. It is seen that the radial distance for initiation of flow separation increases with the decrease in the buoyancy parameter. This is very reasonable because a duct with a lower wall-heat-flux at a fixed rotating speed condition requires a longer radius of the radial ration for reaching enough against buoyancy to drive the fluid upstream.

Comparison with previous experimental results

Figure 10 depicts the effects of the buoyancy parameter, $(Gr/Re^2)[(x + x_0)/De]$, on the Nu_x/Nu_s for the leading and trailing surfaces at several selected axial stations in the radial-inward and radial-outward channels. The experimental data of Wagner *et al.*[15] in the second and the third passages of a serpentine

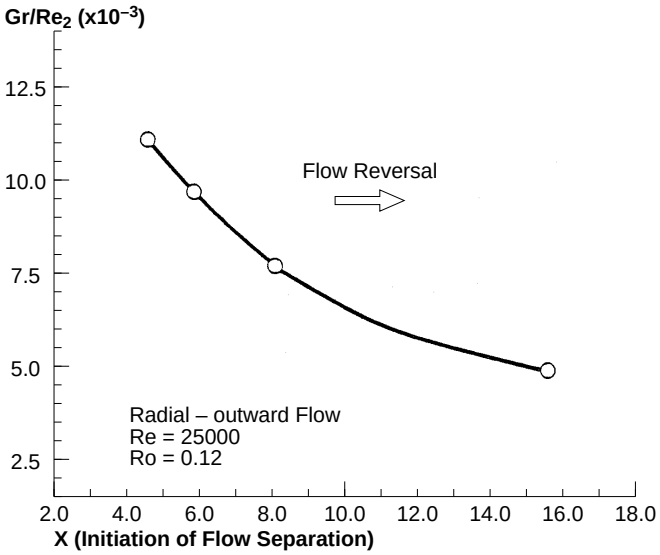

Figure 9.
The relationship between the buoyancy parameter and the radial distance for the initiation of flow separation in the radially outward flow duct

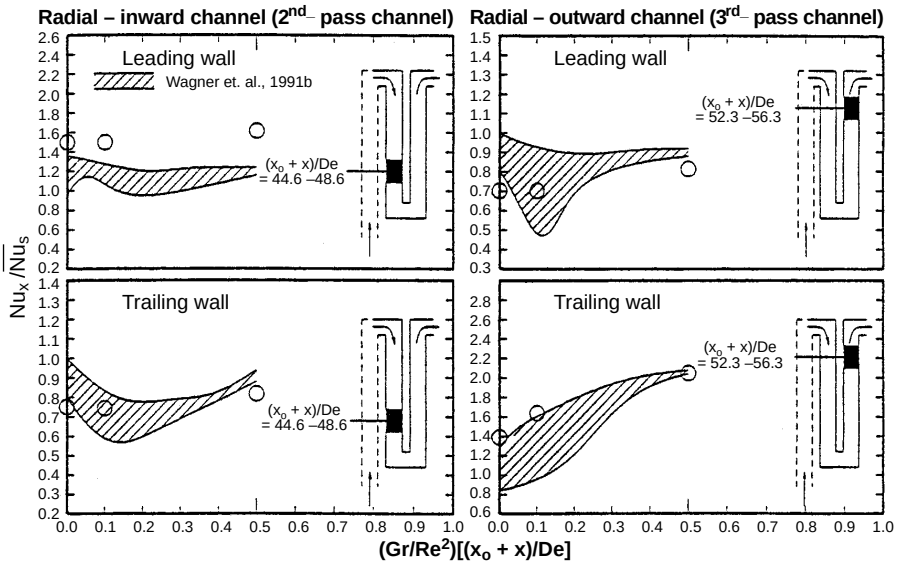

Figure 10.
Comparison of the present numerical and previous experimental results under various rotating buoyancy conditions

rotating channel are plotted as shed bands in Figure 10 for comparison. Note that the present study is under constant wall heat flux, while the study of Wagner *et al.*[11] utilizes uniform wall temperature, and both use a square flow channel. Note also should be taken that the results conducted by Wagner *et al.*[11] are based on the regionally averaged Nusselt number, which averages over a test segment with about four channel hydraulic diameters in length. Therefore, the Nusselt number deduced in the present work for comparison is averaged over 4*De* in channel length in the vicinity of the same radial station as the experiment related to the rotating axis. It is seen in this figure that the present calculation agrees reasonably well with the experiments on both the leading and trailing walls of the radial-outward flow channel, but overpredicts in Nusselt number ratio on the leading surface of the radial-inward-flow channel. The general over-prediction of the Nusselt number on the pressure side (although slightly in the radially outward flow) may be due to the difference in the channel length between the present calculation and the previous experiment.

Summary and conclusions

A numerical study of turbulent fluid flow and heat transfer in a periodic two-pass channel with radial rotation has been presented. A standard k-ε turbulence model including not only the Coriolis and rotational buoyancy effects in the momentum equations but also the modified turbulence production and dissipation due to the Coriolis and buoyancy effects in the k and ε transport equations has been employed to resolve this problem. Satisfactorily reasonable predictions have been achieved by comparing the present calculation with the

available experiments. Basically, the rotational buoyancy effects can alter the axial velocity distribution, change the cross-flow patterns (including the strength and core position of the secondary flow) through coupling of continuity, and modify the turbulent transportation. The combination of all the above effects are found to influence markedly on the local heat transfer in radial-outward flowing channels, but insignificantly in the radial-inward-flow channels. The other main findings from the calculation are summarized as follows:

(1) In the buoyancy-free case, owing to secondary flow induced by the Coriolis force, the heat transfer coefficient in the radial-inward-flow channel diminishes on the trailing surface, but increases on the leading surface. The trend is reversed in the radial-outward-flow channel.

(2) Rotational buoyancy alternates significantly the local heat transfer for the radially outward flow but relatively insignificantly for radially inward flow. The different heat transfer behaviors are mainly attributed to different mechanisms of Coriolis and buoyancy interaction.

(3) In the radial-outward-flow channel, the against buoyancy accelerates the relatively cooled fluid near the trailing surface, and decelerates the relatively warm fluid near the leading surface. Once the rotational buoyancy is sufficiently strong, the decelerated axial fluid will be separated from the leading surface and, in turn, flow reversal over the leading surface. Significantly poor heat transfer is found in the region of initiation of flow separation due to the nearly stagnant fluid. It is further found that the radial distance for initiation of flow separation is decreased by increasing the buoyancy parameter.

(4) Although rotating buoyancy has a great effect on the local heat transfer performance along each channel wall, it has little effect on the channel averaged heat transfer coefficients for the rotational buoyancy investigated. This is because the flow and thermal conditions have been largely developed by complex interaction of the Coriolis and the flow behavior around the 180° sharp bend; hence, additional disturbance introduced by buoyancy, even yielding reversed flow, can not alter too much the overall performance.

References

1. Majumdar, A.K., Pratap, V.S. and Spadling, D.B., "Numerical computation of flow in rotating ducts", *Trans. ASME, J. Fluids Engineering,* Vol. 99, 1977, pp. 148-53.
2. Howard, J.H.G., Patankar, S.V. and Bordynuik, R.M., "Flow prediction in rotating ducts using Coriolis-modified turbulence model", *Trans. ASME, J. Fluids Engineering,* Vol. 102, 1980, pp. 456-61.
3. Launder, B.E., Tselepidakis, D.P. and Younis, B.A., "A second-moment closure study of rotating channel flow", *J. Fluid Mechanics,* Vol. 183, 1987, pp. 63-75.
4. Iacovides, H. and Launder, B.E., "Parametric and numerical study of fully developed flow and heat transfer in rotating rectangular ducts", *Trans. ASME, J. Turbomachinery,* Vol. 113, 1991, pp. 331-8.

5. Prakash, C. and Zerkle, R., "Prediction of turbulent flow and heat transfer in a radially rotating square duct", *Trans. ASME, J. Turbomachinery,* Vol. 114, 1992, pp. 835-46.
6. Tekriwal, P., "Heat transfer predictions with extended k-ε turbulence model in radial cooling ducts rotating in orthogonal mode", *Trans. ASME, J. Heat Transfer,* Vol. 116, 1994, pp. 369-80.
7. Bo, T., Iacovides, H. and Launder, B.E., "Developing buoyancy-modified turbulent flow in ducts rotating in orthogonal mode", *Trans. ASME, J. Turbomachinery,* Vol. 117, 1995, pp. 474-84.
8. Wagner, J.H., Johnson, B.V. and Hajek, T.F., "Heat transfer in rotating passages with smooth walls and radial outward flow", *Trans. ASME, J. Turbomachinery,* Vol. 113, 1991, pp. 42-51.
9. Dutta, S., Anderson, M. and Han, J.C., "Prediction of turbulent heat transfer in rotating smooth square ducts", *Int. J. Heat Mass Transfer,* Vol. 39, 1996, pp. 2505-14.
10. Han, J.C. and Zhang, Y.M., "Effect of uneven wall temperature on local heat transfer in a rotating square channel with smooth walls and radial outward flow", *Trans. ASME, J. Heat Transfer,* Vol. 114, 1992, pp. 850-8.
11. Wagner, J.H., Johnson, B.V. and Kopper, F.C., "Heat transfer in rotating serpentine passages with smooth walls", *Trans. ASME, J. Turbomachinery,* Vol. 113, 1991, pp. 321-30.
12. Yang, W.J., Zhang, N. and Chiou, J., "Local heat transfer in a rotating serpentine flow passage", *Trans. ASME, J. Heat Transfer,* Vol. 114, 1994, pp. 354-61.
13. Patankar, S.V., Liou, L.H. and Sparrow, E.M., "Fully developed flow and heat transfer ducts having periodic variations of the cross-section area", *Trans. ASME, J. Heat Transfer,* Vol. 99, 1977, pp. 180-6.
14. Launder, B.E. and Spalding, D.B., "The numerical computation of turbulent flow", *Computer Methods in Applied Mechanics and Engineering,* Vol. 3, 1974, pp. 269-89.
15. Hossian, M.S. and Rodi, W., "A turbulence model for buoyant flows and its application to vertical buoyant jets", in Rodi, W. (Ed.), *Turbulent Buoyant Jets and Plumes,* pp. 143-46, Pergamon Press, New York. Vol. 102, 1982, pp. 456-61.
16. Patankar, S.V., *Numerical Heat Transfer and Fluid Flow,* Hemisphere, Washington, DC, 1980.
17. Liou, T.M., Hwang, J.J. and Chen, S.H., "Turbulent transport phenomena in a channel with periodic rib turbulators, *AIAA, J. Thermophysics,* Vol. 6, pp. 513-21.
18. Taylor, A. Whitelaw, J.H. and Yianneskis, M., "Curved ducts with strong secondary motion: velocity measurements of developing laminar and turbulent flow", *Trans. ASME, J. Fluids Engineering,* Vol. 104, 1982, pp. 350-9.
19. Choi, Y.D., Icaovides, H. and Launder, B.E., "Numerical computation of turbulent flow in a square 180-deg bend", *Trans. ASME, J. Fluids Engineering,* Vol. 111, 1989, pp. 59-68.